Mapping Woody Cover in Semi-arid Savannahs using Multi-seasonal Composites from Landsat Data

Thomas P Higginbottom [a*], Elias Symeonakis[a], Hanna Meyer[b] and Sebastian van der Linden[c]

[a] School of Science and the Environment, John Dalton Building, Manchester Metropolitan University, Manchester, M1 5GD, United Kingdom
[b] Environmental Informatics, Faculty of Geography, Philipps- Universität Marburg, Marburg, Germany
[c] Geography Department, Humboldt-Universität zu Berlin, Berlin, Germany

*Corresponding Authour: T.Higginbottom@mmu.ac.uk, Room 418 John Dalton East.

Abstract

Increasing attention is being directed at mapping the fractional woody cover of savannahs using Earth-observation data. In this study, we test the utility of Landsat TM/ ETM-based spectral-temporal variability metrics for mapping regional-scale woody cover in the Limpopo Province of South Africa, for 2010. We employ a machine learning framework to compare the accuracies of Random Forest models derived using metrics calculated from different seasons. We compare these results to those from fused Landsat-PALSAR data to establish if seasonal metrics can compensate for structural information from the PALSAR signal. Furthermore, we test the applicability of a statistical variable selection method, the recursive feature elimination (RFE), in the automation of the model building process in order to reduce model complexity and processing time. All of our tests were repeated at four scales (30, 60, 90, and 120 m-pixels) to investigate the role of spatial resolution on modelled accuracies.

Our results show that multi-seasonal composites combining imagery from both the dry and wet seasons produced the highest accuracies (R^2= 0.77, RMSE=9.4, at the 120 m scale). When using a single season of observations, dry season imagery performed best (R^2=0.74, RMSE=9.9, at the 120 m

resolution). Combining Landsat and radar imagery was only marginally beneficial, offering a mean relative improvement of 1% in accuracy at the 120 m scale. However, this improvement was concentrated in areas with lower densities of woody coverage (<30%), which are areas of concern for environmental monitoring. At finer spatial resolutions, the inclusion of SAR data actually reduced accuracies. Overall, the RFE was able to produce the most accurate model (R^2=0.8, RMSE=8.9, at the 120 m pixel scale). For mapping savannah woody cover at the 30 m pixel scale, we suggest that monitoring methodologies continue to exploit the Landsat archive, but should aim to use multi-seasonal derived information. When the coarser 120 m pixel scale is adequate, integration of Landsat and SAR data should be considered, especially in areas with lower woody cover densities. The use of multiple seasonal compositing periods offers promise for large-area mapping of savannahs, even in regions with a limited historical Landsat coverage.

Keywords:

- Landsat-metrics;
- Optical-radar fusion;
- woody cover mapping;
- Savannahs;
- Large-area mapping

1 Introduction

Savannah ecosystems are characterised by a dynamic mosaic of tree, shrub and grass species. Variations in these components can result in widely divergent ecological functions (Sankaran et al., 2005). There is growing concern over the health and sustainability of savannahs across the world. Increases in shrub cover at the expense of grasslands (i.e. shrub encroachment) have been reported in semi-arid environments globally (Naito and Cairns 2011, Stevens et al., 2016, Tian et al., 2016, Skowno et al., 2017). In contrast, overexploitation of woody shrubs and trees for fuelwood may be depleting woody cover in other regions (Wessels et al., 2013, Brandt et al., 2017).

Monitoring savannahs is a challenging endeavour, and due to the discontinuous nature of land cover in such environments, categorical maps are of limited value. Alternatively, representing the 2-dimension horizontal woody cover component as a continuous fractional layer is more ecologically relevant, and recent advances in the field have focused their attention to this characteristic (Bucini et al., 2010, Armston 2009, Naidoo et al., 2016). However, the spatial heterogeneity of savannahs makes fractional cover modelling vulnerable to scale effects, as areas of very high or low coverage will be lost by aggregation to coarser scales (Guerschman et al., 2009). Therefore, it is necessary to consider analyses over a range of resolutions, enabling an optimum balance between model accuracy and spatial detail to be established (Urbazaev et al., 2015).

Passive optical Earth observation (EO) data, such as Landsat, have commonly been employed to map savannah vegetation in the past (Prince and Astle 1986). Such data discriminate vegetation type by exploiting the full spectral range of reflected solar radiation. Passive optical data also allow for vegetation indices, such as the Normalized Difference Vegetation Index (NDVI), to be used as proxies of various biogeophysical parameters, such as net primary productivity (NPP), fraction of photosynthetically active radiation (fPAR), and leaf area index (LAI) (Carlson and Ripley 1997, Higginbottom and Symeonakis 2014, Zhu et al., 2013). Yet single date optical imagery can be inappropriate for discriminating woody and grass coverage, as photosynthetic activity is detected indiscriminately (Olsson, Leeuwen, and Marsh 2011). In savannahs, the woody cover component decreases temporal variation within the NDVI signal, as bushes and shrubs maintain leaves throughout the dry season (Bucini et al., 2010, Naidoo et al., 2016). Information derived from a pixel-level time series can therefore contain valuable information for land cover mapping. If sufficient observations are available, phenological metrics detailing the start and end points of seasons can be calculated (Brandt et al., 2016). Alternatively, spectral-temporal variability metrics from single spectral bands or indices (e.g. minimum, maximum, mean, median, etc.) can quantify variability even in regions with lower observation densities (Müller et al., 2015, Zhong, Gong, and Biging 2014).

Irrespective of processing method, optical data possesses fundamental limitations for mapping woody environments, because it does not directly correlate to surface structure (Naidoo et al., 2016). Active EO sensors such as Synthetic Aperture Radar (SAR) provide information on the 3-dimensional structure of the land surface, by emitting microwaves and measuring the intensity of energy reflected back to the sensor after interactions with ground objects i.e. the *backscatter* (σ^0) of the signal. The use of SAR data in fractional woody cover mapping, particularly L-band, operating with wavelengths of 0-15 cm , has been well demonstrated (Bucini et al., 2010, Mathieu et al., 2013, Naidoo et al., 2015, 2016). Mitchard et al., (2009) identified a consistent relationship between cross-polarised L-band backscatter and aboveground biomass (AGB) across four pan-African tropical savannahs, regardless of vegetation composition. Advanced Land Observing Satellite (ALOS) Phased Array type L-band Synthetic Aperture Radar (PALSAR) imagery has been highlighted as the most reliable satellite-based indicator of both AGB and canopy coverage for woody cover in semi-arid savannahs (Naidoo et al., 2015, 2016). However, the use of L-band imagery for mapping long-term land cover change is affected by a number of data continuity issues, sensor failures (JERS-1, ALOS PALSAR), high data costs, and the short lifespan of radar systems, resulting in a limited temporal archive compared to Landsat. There are less limitations when using C-band radar, such as Radarsat or Sentinel-1, due to more consistent coverage (Reiche et al., 2016). However, C-band radar is not as sensitive to woody cover, compared to L-band (Mathieu et al., 2013).

More recently, the fusion of optical and radar imagery has been shown to provide an improvement upon single-sensor fractional cover accuracies (Bucini et al., 2010, Naidoo et al., 2016). Bucini et al., (2010) and Naidoo et al., (2016) combined L-band radar data with Landsat to map woody canopy coverage in the Kruger National Park, South Africa: the fusion approach improved the accuracy over single sensor predictions, particularly when combining SAR with multi-season imagery. Lucas et al., (2006) used PALSAR thresholds in conjunction with Landsat-derived Foliage Projected Cover maps to successfully discriminate regrowth stages in open Eucalyptus forests. Merging various SAR wavebands, such as C, X, or L, have also been shown to provide benefits for woody cover mapping,

105 although these improvements were found to be smaller (~3%) when compared with L-band alone
106 (Naidoo et al., 2015). Choosing the appropriate sensor, or combination of sensors, for woody cover
107 mapping, is therefore an increasingly complex decision with further study required.

108 The increasing number and variety of EO systems in operation, coupled with open-data policies,
109 presents a wide range of pathways for land cover mapping. Compared to earlier investigations, it is
110 now routine for studies to use high-dimensional data. However, this approach comes with statistical
111 limitations. Predictive models trained using high-dimensional data are prone to overfitting, thus
112 transferring poorly to unseen validation data. This issue is important, potentially incurring a high
113 degree of variance into classifications, whilst reducing bias (i.e. the bias-variance dilemma) (James et
114 al., 2013, Kuhn and Johnson 2013). A number of techniques exist to process high-dimensional data
115 and extract the most relevant variables, aiming to reduce model complexity whilst retaining predictive
116 accuracy (Guyon et al., 2002, Guyon and Elisseeff 2003). To date the implementation of these methods
117 in remote sensing analyses has been limited (Meyer et al., 2016), but may be increasingly beneficial in
118 the near future as the number of data sources continues to increase.

119 Within this context, the overarching aim of this study is to develop a framework for accurately
120 mapping the fractional woody cover of semi-arid savannahs at large spatial scales, using freely and
121 widely available data sources. We address this overarching aim by carrying out a multi-scale
122 comparative exercise that provides answers to the following questions:

123 1. Can annual time series of Landsat metrics be used to accurately map fractional woody cover,
124 and to what extent does seasonality of the compositing period influence results?
125 2. How do Landsat-based estimates compare to multi-sensor fusion approaches combining L-
126 band SAR data?
127 3. Can automated variable selection methods, such as Recursive Feature Elimination, assist in
128 reducing the number of variables used without compromising accuracy?

2 Study Area

Our study area is the Limpopo Province, South Africa (Fig 1). The province is ~125,000 km^2 and intersects 14 Landsat WRS-2 scenes. This region is predominantly open deciduous savannah and grassland, with discontinuous woody cover ranging from 0-60% coverage (Mucina and Rutherford 2006). The climate is mainly semi-arid with small humid subtropical areas (Kottek et al., 2006). Mean annual temperatures range from 21-23°C and winters are mild and frost-free (Scholes et al., 2001). Rainfall increases along a north-south gradient, with mean annual precipitation of 450 mm/year in the north, rising to 700 mm/year in the south (Scholes et al., 2001). The majority of rainfall occurs in the winter months (October to March; Fig 2).

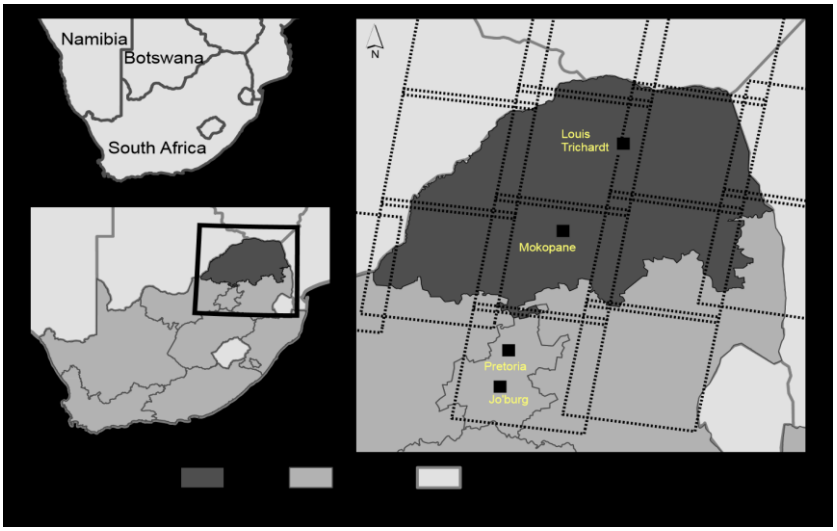

Figure 1: Location of the study area, the Limpopo Province of South Africa

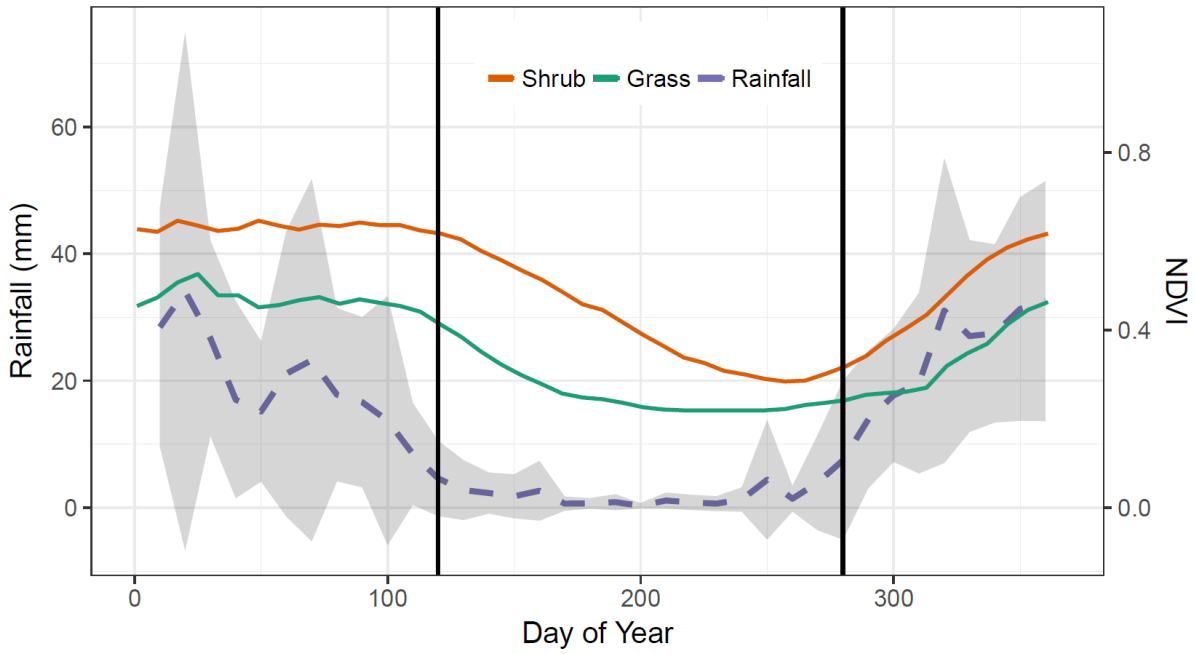

Figure 2: Annual seasonality of NDVI for a dense shrub and grassland pixel, and regional rainfall for the Limpopo Province. NDVI is the mean value from 15 year of MODIS-MCD43A4 16 day observations, rainfall data is the mean and standard deviations from FEWS-NET (https://www.fews.net/). The vertical lines indicate the start and the end of the dry season.

There are pronounced contrasts in land use intensity across the region. In the east, the Kruger National Park is the largest protected area in South Africa featuring minimal human usage beyond fire experiments and animal enclosures. This contrasts with the communally governed areas originating from apartheid-era homelands (Worden 2012). These areas generally feature very high population densities ranging from 200-300 people per km^2, resulting from forced resettlement in the 1960-1990 apartheid period (Pollard et al., 2003). Consequently, overgrazing and unsustainable wood harvesting are widespread with many areas classified as degraded (Wessels et al., 2013).

3 Data

3.1 Training and validation data

We aimed to develop a transferable method for woody cover mapping. Accordingly, we used training and validation data from aerial imagery, so that our methodological framework would be applicable in study areas where such imagery is available but other data may not be or are costly, e.g. field surveys, Lidar. In South Africa, the National Geospatial Information (NGI) agency of the Department of Rural Development and Land Reform have been providing 0.5 m colour aerial photography since 2008 , with an orthoreftification accuracy of ±3 m (NGI 2017) . Six 5×5 km images were selected according to a stratified approach based on mean annual precipitation, with acquisition dates between the 19th April and 7th August of the years 2008 and 2009 (Appendix 1).

3.2 Satellite imagery

3.2.1 Landsat

Spectral-temporal variability metrics are a method of capturing information on the temporal evolution of spectral values within a pixel (Muller et al., 2016). We hypothesised that metrics capturing this variability would be effective for woody cover monitoring. To generate metrics, all available Landsat 5 and 7 images that intersected the Limpopo Province for 2009-2010 were used, for the wet season additional images from the two neighbouring hydrological years were also used (scene footprints shown in Fig 1). Top-of-atmosphere (TOA) reflectance was calculated using standard bias-gain equations. Pixels affected by clouds or cloud shadow were removed based on the F-mask algorithm (Zhu and Woodcock 2012), no correction was applied for missing Scan Line Corrector (SLC-off) pixels. For each pixel, all co-located observations were used to calculate the following statistics: mean, median, minimum, maximum, and standard deviation. These metrics were calculated over three time-periods: annual, dry season and wet season (Fig 2), resulting in a total of 90 Landsat-

derived layers. The number of images used within each observation period is given in Table 1. Due to persistent high cloud cover, wet season metrics were calculated over three southern hemisphere hydrological years. Processing was undertaken in the Google Earth Engine cloud computing environment (Gorelick et al., 2017, Moore and Hansen, 2011).

Period	Start Date	End Date	Landsat 5 Images	Landsat 7 Images	Total Images
Annual Cycle	1st January	31st December	86	259	345
Dry Season	1st November	30th April	52	186	238
Wet Season	1st May	1st October	27	102	129
Total Unique Images			88	324	412

Table 1: Number of Landsat images used in each period for variability metric calculations. Wet season metrics are calculated over three hydrological years: 2009-2010, 2010-2011, and 2011-2012. *Total Unique* does not equal the sum of rows as images can be included in both a single season and the annual period.

3.2.2 ALOS-PALSAR

ALOS PALSAR, and its successor ALOS-2 PALSAR-2, are fully polarimetric L-band Synthetic Aperture Radar systems (Rosenqvist et al., 2007). These sensors operate at a wavelength of 23.6 cm. We used the 2010 data from the ALOS PALSAR global mosaic, a science-ready product generated annually for 2007 to 2010 (ALOS), and 2015 (ALOS-2). The images for this mosaic were from the dry season, with acquisition dates between 1st July - 3rd October and two images from 2009. Dual polarization HH (horizontal-horizontal) and HV (horizontal-vertical) backscatter data were used. Pre-processing of the input raw imagery includes orthorectification using the Shuttle Radar Topography Mission (SRTM)

Digital Elevation Model (DEM), calibration, speckle reduction, and a destriping procedure (Shimada and Ohtaki 2010, Shimada et al., 2014). The raw digital number format was converted to backscatter (σ^0) using the calibration equation:

$$\sigma^0 = 10 * log_{10}(DN + 0.001)^2 + CF \quad (1)$$

where DN is the raw digital number and CF is a calibration factor (=-83). The 25 m mosaic was resampled to match the Landsat resolution using bilinear resampling.

4 Methods

The methodological framework is shown in Fig 3. To establish the optimum approach for fractional woody cover mapping, we ran a series of random forest regressions to compare the accuracies achieved from single season Landsat metrics, multi-season data, or multi-sensor combining Landsat and SAR data. These models were repeated at four resolutions: 30, 60, 90 and 120 m, to ascertain the ideal scale for large-area monitoring. Processing was undertaken in the *R* Statistical Software Environment, using the *raster*, *caret,* and *randomForest* packages (Hijmans et al., 2015, Kuhn 2015, Liaw and Wiener 2002, *R* Core Team 2015). Fractional cover sampling code was adapted from Leutner and Horning (2016).

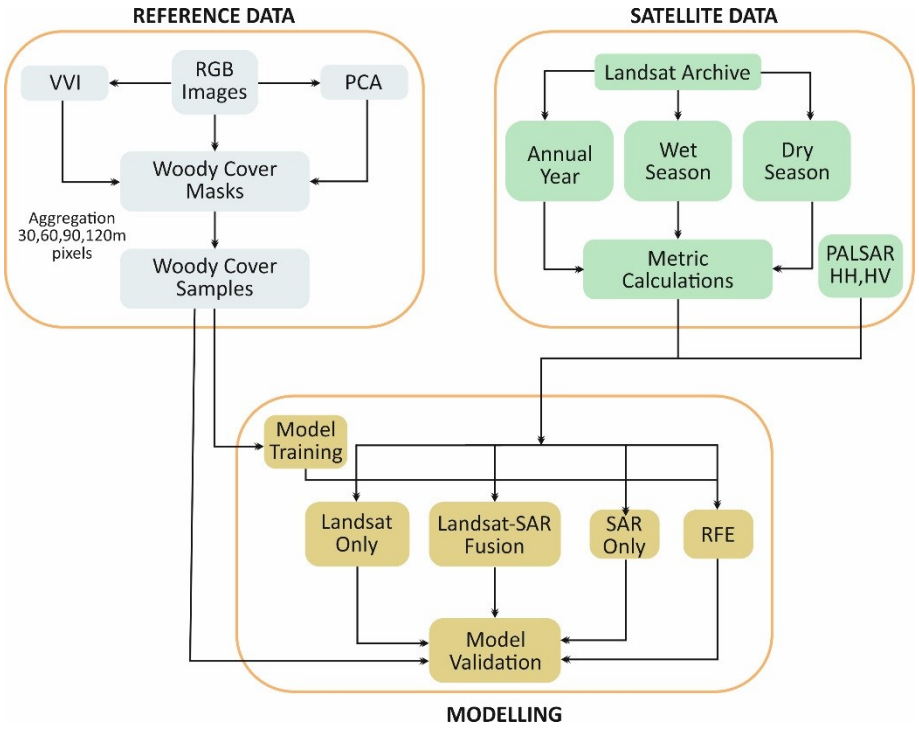

Figure 3. Flow chart of methodological framework. VVI: Visible Vegetation Index; PCA: Principle Components Analysis; RFE: Recursive Feature Elimination.

4.1 Creation of Reference Data

To create training data the six aerial imagery subsets were classified into woody/non woody masks. We opted for aerial image classification to enable methods to be transferable to other locations, due to the generally satisfactory availability of aerial imagery at appropriate scales (Staben et al., 2016). Firstly, a principal components analysis (PCA) was applied to the three RGB layers and the first two components were extracted. Secondly, we calculated the visible vegetation index (Joseph and Devadas 2015) which uses visible light spectra to estimate photosynthetic activity and is defined as:

$$VVI = \left[(1 - \frac{R - R_0}{R + R_0})(1 - \frac{G - G_0}{G + G_0})(1 - \frac{B - B_0}{B + B_0})\right] \quad (2)$$

where VVI is the visible vegetation index, *R*, *G* and *B* are the red, green, and blue intensities in the image, R_0, G_0 and B_0 are values of red, green, blue used to reference green colour (30, 50, and 1, respectively), determined by the image bit rate (Joseph and Devadas 2015).

A Random Forest classifier was used to create the binary woody-non woody layers from the original RGB layers, principle components, and VVI. Individual models were generated for each image using 400 manually selected points per image (75/25% training-validation split). The mean classification accuracy was 85%. Full accuracy statistics are given in the Appendix. An example classified mask is shown in Fig 4.

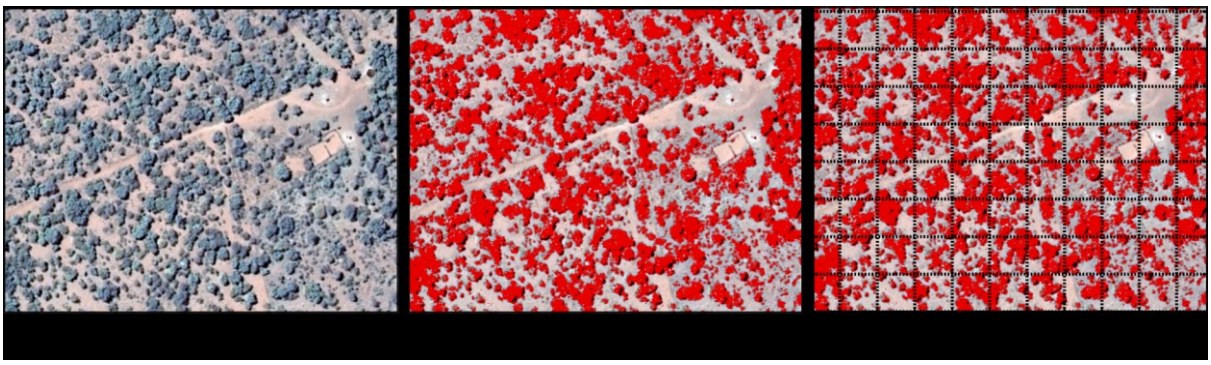

Figure 4: Example of the RGB woody classification. (a) raw RGB image; (b) classified woody cover shown in red, and (c) 30 m grid for fractional cover sampling.

To generate training and validation data for the satellite imagery, Landsat pixel-sized squares (i.e. 30×30 m) were extracted from the woody/non-woody masks and the percentage woody coverage calculated. From each image, $7000/\alpha$ samples were extracted, where α takes the values of 1, 2, 3 or 4, depending on the aggregation level used to test the effect of scale in the accuracy of the woody cover estimates (Fig 3). For example, for a pixel size of 30m, α=1 and the samples extracted from each image are 7000, whereas for an aggregation level of α=2 or a pixel size of 60 m, the number of samples extracted are 7000/2=3500. These samples were merged and split into equal training and validation subsets with equal probability distributions of woody cover (Fig 5). The spatial aggregation process may incur central tendency in training values, with the reduction in high or low samples making the

subsequent regression task easier. To quantify this, we tested for any significant difference between the sample distributions using Pairwise-Wilcoxon tests. These highlighted a significant (p < 0.05) difference between the data at 30 m and all other scales which can also be visualised in the relatively reduced number of high (>75%) and low (<10%) values in the respective aggregated pixel histograms (Figure 5).

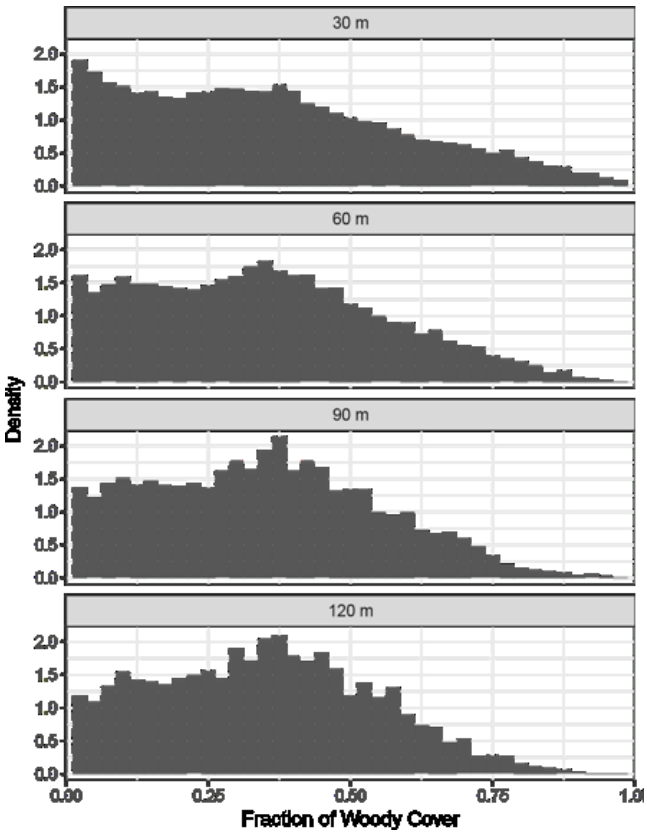

Figure 5: Density histograms of model training values at the four scales tested

4.2 Random Forest Regression

Predictive models were generated using the Random Forest algorithm. Random Forest is an ensemble machine learning procedure that combines bootstrapping and aggregation (bagging) with decision trees (Breiman 2001). All models were individually tuned using 10 repeats of 10-fold cross

validation to identify the ideal parameter specification. This covered the number of variables considered at each tree node and the number of trees constructed.

4.3 Variable Selection

To identify optimum predictive models, we incorporated all potential variables into a variable selection process. According to statistical learning theory, a model containing fewer predictors that is comparably accurate is preferential to a more complex model (James et al., 2013, Kuhn and Johnson 2013). Backwards selection methods are effective in identifying the ideal number of variables for prediction, allowing the selection of the most parsimonious model that offers comparable accuracy (Guyon et al., 2002, James et al., 2013, Kuhn and Johnson 2013). The combination of Landsat metrics and PALSAR data resulted in 92 predictors (90 Landsat metrics + 2 PALSAR backscatter), a number of which are correlated. To identify the most important predictors, we implemented the backwards selection method of recursive feature elimination (RFE). RFE is a parameter selection process that incorporates the estimation of test (validation) errors and variable importance (Guyon et al., 2002). Firstly, a model is constructed using all available predictors (Mp). The test error of this model (i.e. adjusted R^2 and RMSE) is then estimated using 10-fold cross validation, and variable importance scores are calculated. A second model is then established which excludes the lowest contributing variable from Mp, and test error and variable importance are recalculated. This process is repeated until a one-variable model remains. A full iteration of this procedure is repeated 10 times to account for variations in the cross validation sampling, providing a robust estimate of test errors. An ideal model that offers the best performance whilst using the least variables can then be selected.

5 Results

5.1 Woody Cover Mapping

A fractional woody cover map derived from the most accurate model tested, is shown in Fig 6. Subsets comparing the mapped woody cover estimates from a number of models and the NGI aerial imagery are shown in Fig 7.

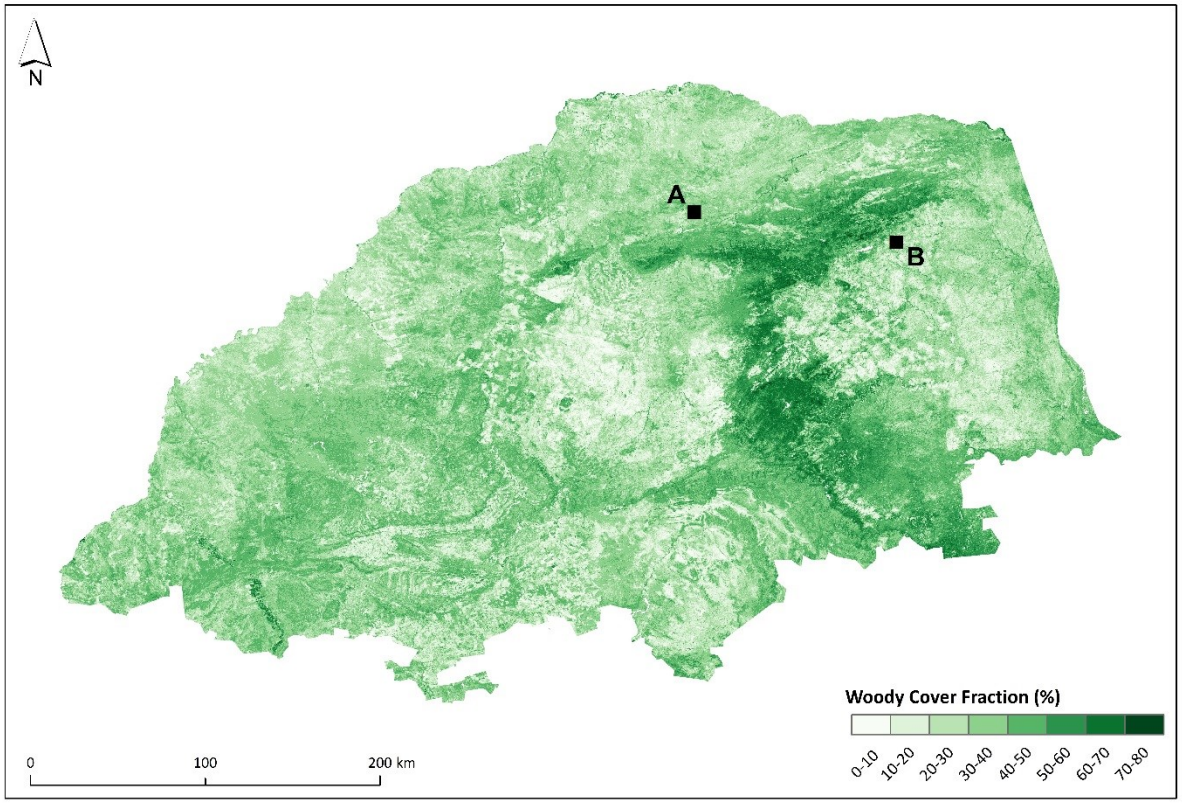

Figure 6. Fractional woody cover results for the Limpopo Province based on the Recursive Feature Elimination model at the 120 m pixel scale. Black squares A and B are the locations of the subsets in Fig 7.

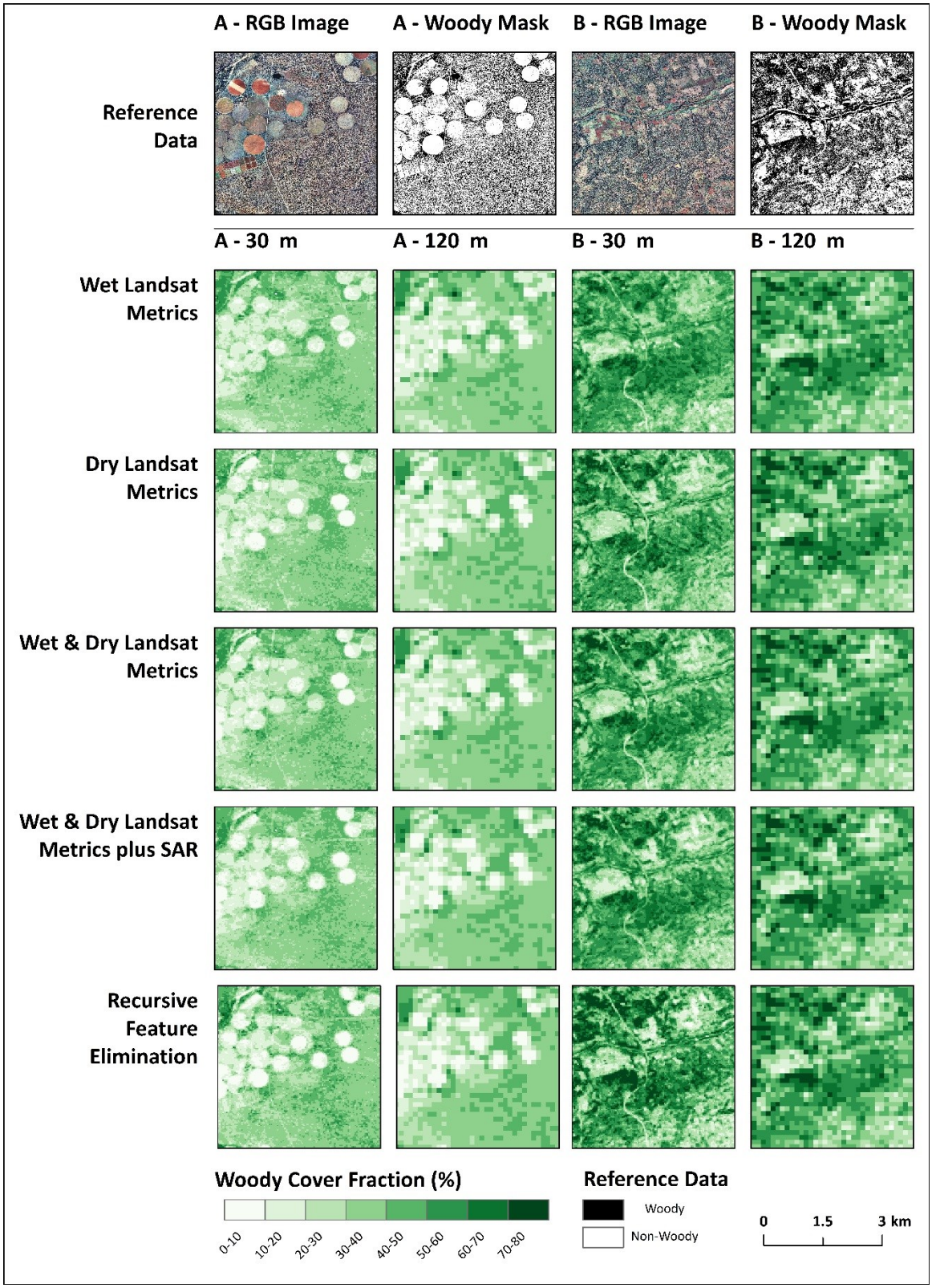

Figure 7. Spatial patterns of woody cover for subsets A and B of Fig 6 at 30 and 120 m pixel scales. Five model predictions and the respective reference aerial imagery from the NGI are shown. Aerial imagery acquisition dates: A: 19 April 2009, B: 30 April 2009.

5.2 Seasonal Landsat models

The performance of Landsat-based models is shown in Fig 8 and Table 2. When using metrics derived from a single season, the highest accuracies were obtained by using the dry season metrics, followed by the full annual cycle, with the wet season performing the worst. This pattern was consistent across all scales (Table 2). Using a combination of metrics derived from two seasons, the highest accuracies came from models incorporating both dry and wet season data, followed by dry and annual, and finally wet and annual (Table 2). Reducing the pixel resolutions (i.e. increasing the aggregation factor), consistently raised the model performances, with the largest improvement occurring in the initial aggregation from 30 m to 60 m.

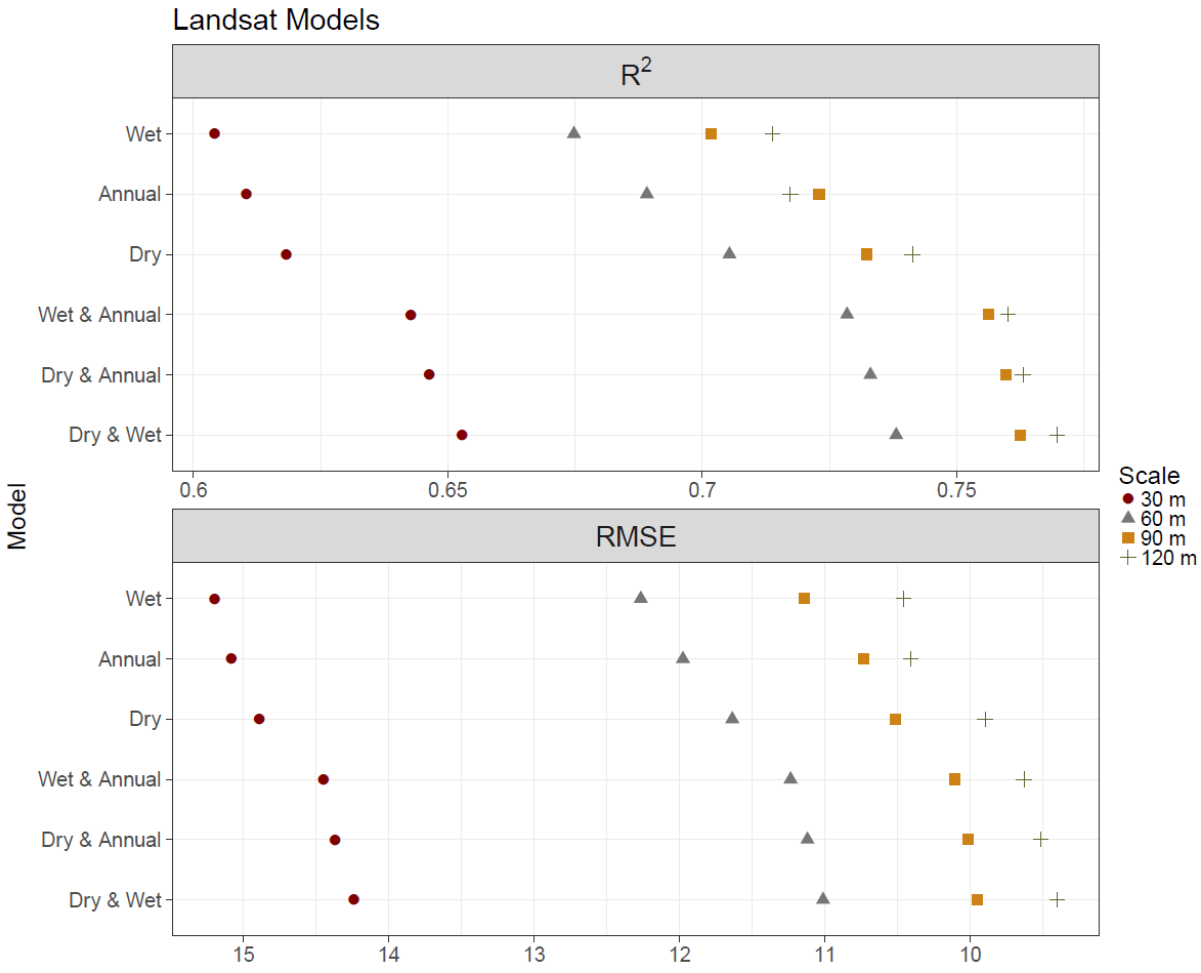

Figure 8. Model accuracy results for Landsat metrics-based models RMSE units are percentage woody cover (0-100%)

	120 m n-3,848		90 m n-6,826		60 m n-10,499		30 m n-21,000	
	R^2	RMSE	R^2	RMSE	R^2	RMSE	R^2	RMSE
Landsat Dry and Wet	0.77	9.4	0.762	10	0.738	11	0.653	14.2
Landsat Dry and Annual	0.763	9.5	0.76	10	0.733	11.1	0.646	14.4
Landsat Wet and Annual	0.76	9.6	0.756	10.1	0.728	11.2	0.643	14.4
Landsat Dry	0.741	9.9	0.732	10.5	0.705	11.6	0.618	14.9
Landsat Annual	0.717	10.4	0.723	10.7	0.689	12	0.61	15.1
Landsat Wet	0.714	10.5	0.702	11.1	0.675	12.3	0.604	15.2

Table 2. Model accuracy results for the Landsat metrics-based models, RMSE units are percentage woody cover (0-100%)

5.3 Fused models

Accuracy statistics from models combining Landsat metrics with ALOS PALSAR backscatter are shown in Fig 9 and Table 3. Overall, the same ranking of seasonal performance as Landsat-only models was observed. For a single season, accuracy decreased from dry to annual to wet, whilst multi-season models were ranked: dry and wet, dry and annual, and wet and annual. The only exception to this order was at the 90 m pixel scale, where the single season annual metrics and dry-annual multi-season models performed best (Table 4).

The fusion of PALSAR backscatter with Landsat metrics had contrasting impacts on model accuracy (Table 4). At the 120 m scale, all models were improved. Conversely, at the 30 m scale, performances were negatively affected. At mid-range scales (60 and 90 m), the single season annual models were improved, as did the 90 m 'wet' model. All other mid-scale models responded negatively to the SAR fusion or were unaffected. At the 120 m scale, the fusion was generally more effective for single season models over multi-temporal combinations. Finally, at all scales, the annual models performed better when used together with the SAR data.

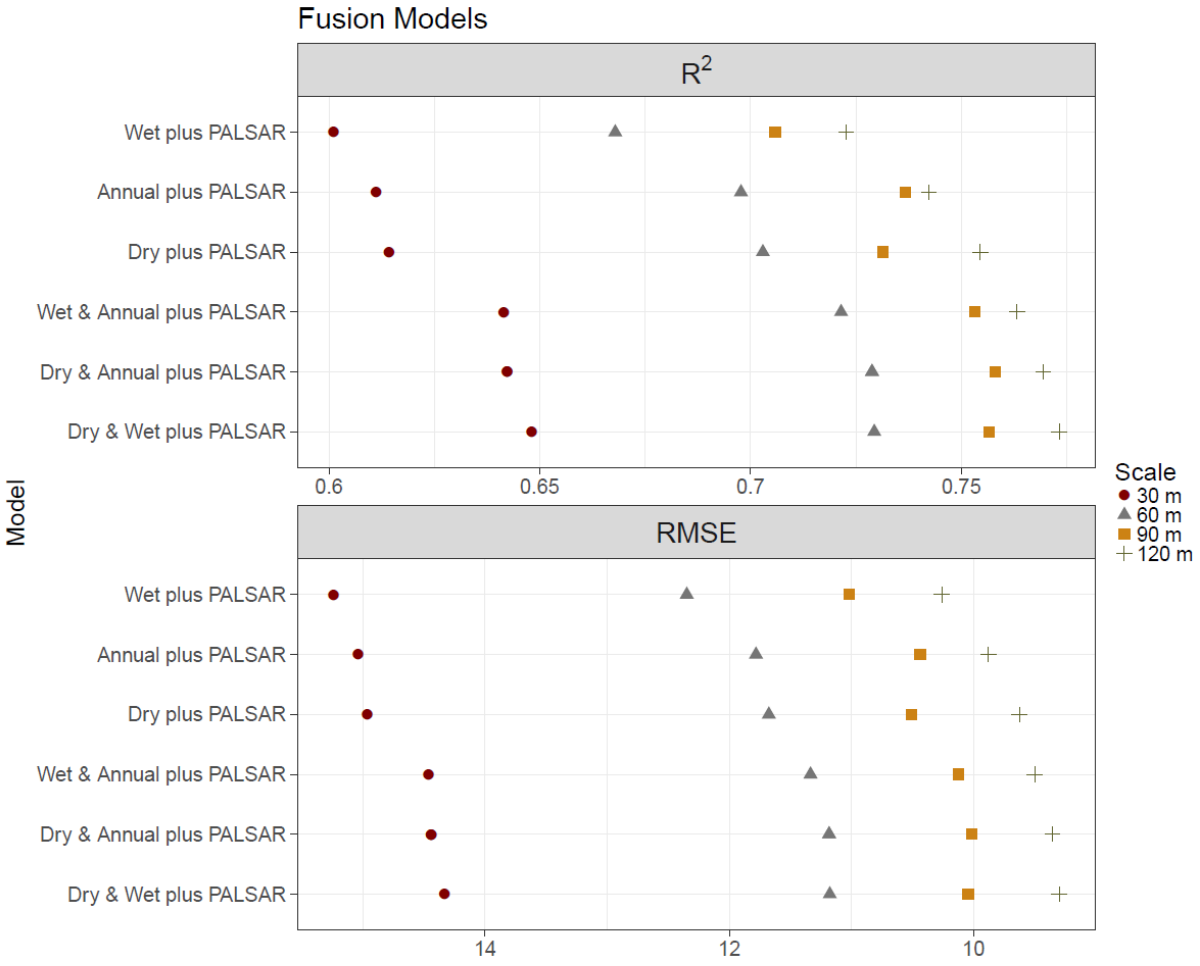

Figure 9: Model accuracies (R^2 and RMSE) for Landsat-PALSAR fusion models

Table 3. Accuracy metrics for Landsat-PALSAR fusion models

	120 m		90 m		60 m		30 m	
	R^2	RMSE	R^2	RMSE	R^2	RMSE	R^2	RMSE
Landsat Dry and Wet	0.773	9.3	0.757	10	0.729	11.2	0.648	14.3
Landsat Dry and Annual	0.769	9.4	0.758	10	0.729	11.2	0.642	14.4
Landsat Wet and Annual	0.763	9.5	0.753	10.1	0.721	11.3	0.641	14.5
Landsat Dry	0.755	9.6	0.731	10.5	0.703	11.7	0.614	15
Landsat Annual	0.742	9.9	0.737	10.4	0.698	11.8	0.611	15
Landsat Wet	0.723	10.3	0.706	11	0.668	12.3	0.601	15.2
PALSAR Only	0.37	15.5	0.313	16.9	0.25	18.7	0.180	22.2

Table 4. Difference between the Landsat only and Landsat-PALSAR fusion models. Green numbers indicate improvement from the fusion while red the opposite.

	120 m		90 m		60 m		30 m	
	R^2	RMSE	R^2	RMSE	R^2	RMSE	R^2	RMSE
Landsat Dry and Wet	0.003	-0.1	-0.5	0	-0.9	0.2	-0.005	0.1
Landsat Dry and Annual	0.006	-0.1	-0.2	0	-0.4	0.1	-0.004	0
Landsat Wet and Annual	0.003	-0.1	-0.3	0	-0.7	0.1	-0.002	0.1
Landsat Dry	0.014	-0.3	-0.1	0	-0.2	0.1	-0.004	0.1
Landsat Annual	0.025	-0.5	1.4	-0.3	0.9	-0.2	0.001	-0.1
Landsat Wet	0.009	-0.2	0.4	-0.1	-0.7	0	-0.003	0

5.4 Recursive Feature Elimination (RFE)

The accuracy results from the RFE automated variable selection approach is shown in Fig 10. At all scales, model accuracies were higher when more than 25 variables where included in the model and performance declined rapidly when fewer than that were considered. The optimal number of variables to balance predictive accuracy and model simplicity was established as 57 for the 120 m-pixel scale, 54 for the 90 m, 70 for the 60 m, and 85 for the 30 m, the top five variable for each model are shown in Table 6. Applying a threshold of two standard errors, based on the cross validations samples for the best model, allows similarly performing models to be compared (James et al., 2013). These models ranged from the one that includes all 92 layers to a minimum of 14 variables for the 120 m scale, 20 for the 90 m scale, 29 for the 60 m, and 39 for the 30 m scale. At all scales, the model constructed by the RFE was the best preforming (Fig 11), providing an improvement in the achieved R^2 of at least 0.012 (Table 5). The 120m scale RFE model was the overall most accurate (Fig 6). To compare the within model variation in accuracy, Figure 12 shows class accuracy statistics for 10% intervals of woody cover

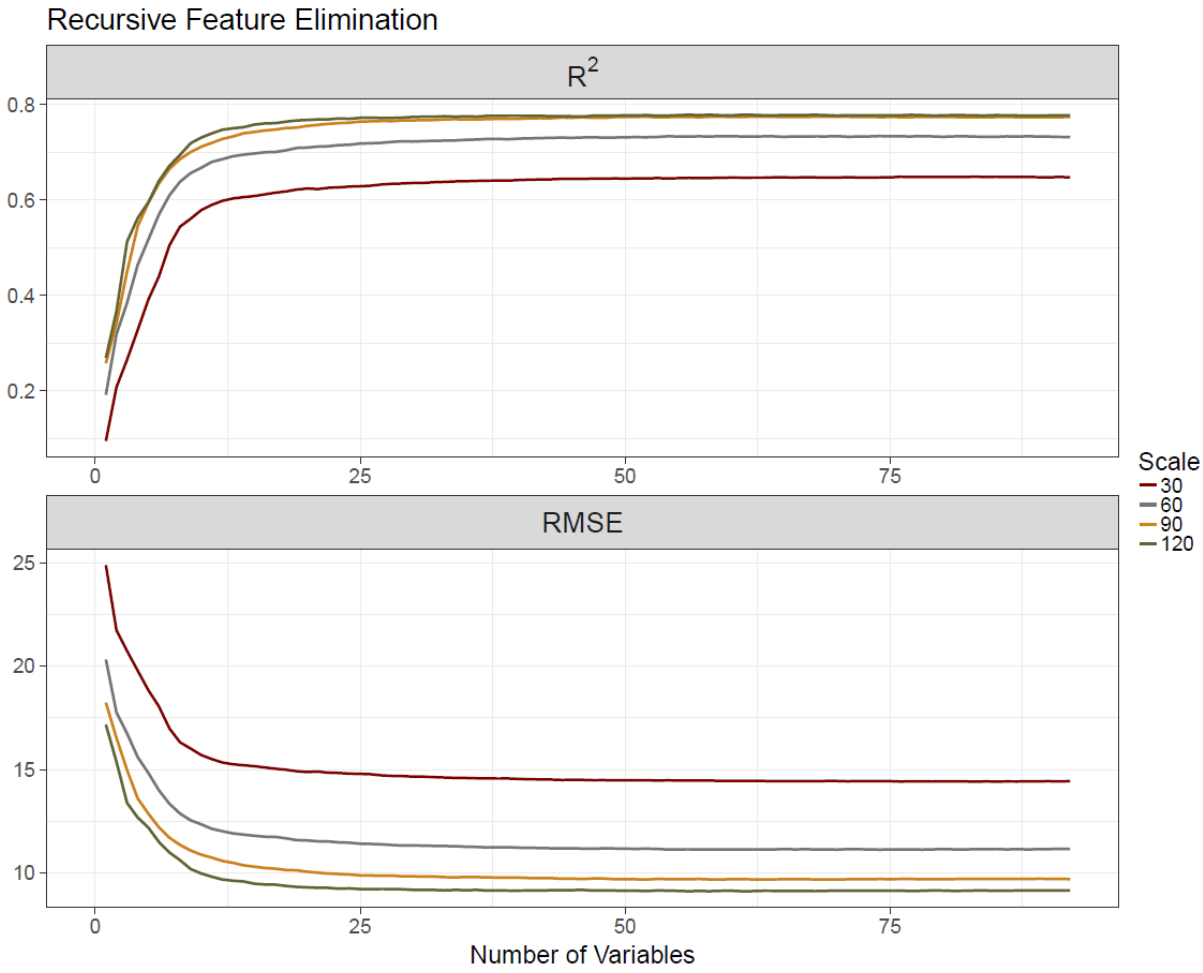

342

343 Figure 10: Cross-validated R^2 and RMSE results from the recursive feature elimination (RFE)

344 process

345 Table 5. Accuracy metrics for the model produced by the recursive feature elimination (RFE), all

346 92 variables, and the best Landsat-only and Landsat-SAR fused combinations.

	120 m		90 m		60 m		30 m	
	R^2	RMSE	R^2	RMSE	R^2	RMSE	R^2	RMSE
Recursive Feature Elimination	0.789	8.9	0.777	9.7	0.75	11.	0.661	14.2
All 92 Variables	0.778	9.2	0.767	9.8	0.741	11.	0.655	14.2
Landsat Dry and Wet	0.77	9.4	0.762	10	0.738	11.	0.653	14.2
Landsat Dry and Wet + SAR	0.773	9.3	0.757	10	0.729	11.2	0.648	14.3

347

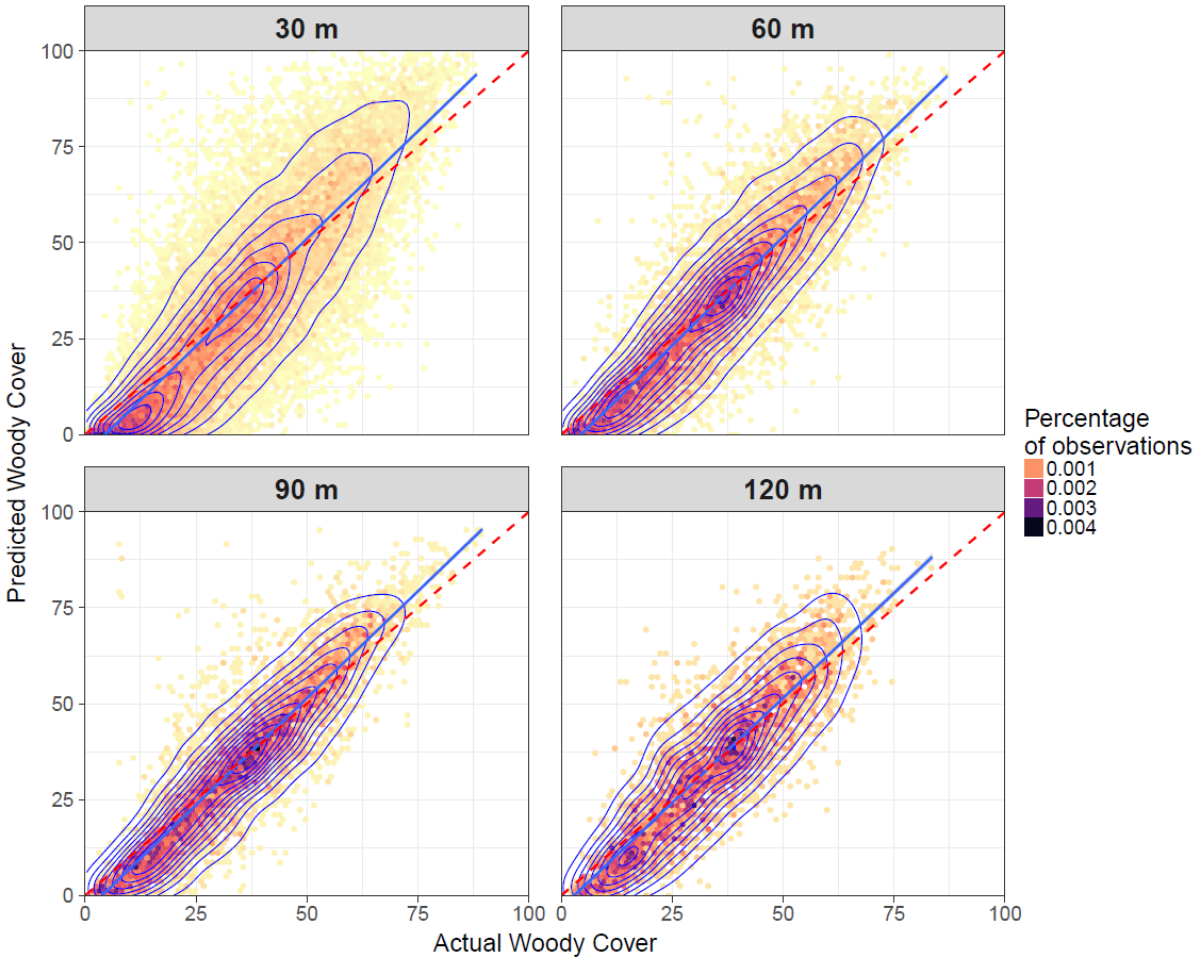

348

349 Figure 11 Density scatter plot of the Recursive Feature Elimination models at the four resolutions

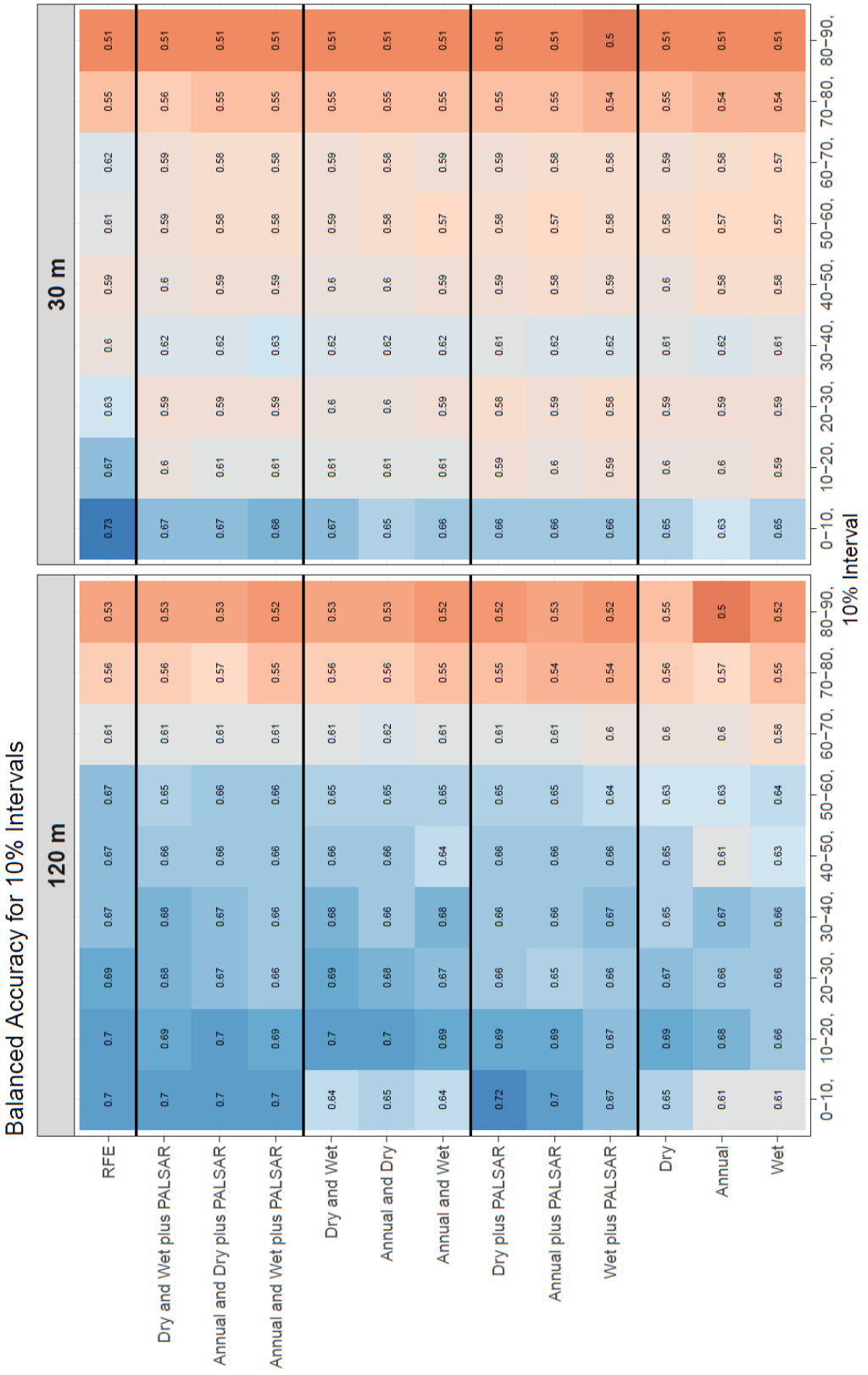

Figure 12. Balanced accuracy figures for the different 120 and 30 m-scale models and woody cover density classes, the original continuous woody cover values were binned into 10% intervals. RFE-Recursive Feature Elimination model.

	30 m	60 m	90 m	120 m
1	**HH**	HH	HV	HV
2	**B1 SD Dry**	B1 SD Dry	HH	HH
3	**B2 SD Dry**	B4 SD Dry	B4 Median Annual	B3 Median Annual
4	**B4 Median Wet**	HV	B3 Median Dry	B5 Median Dry
5	**B4 SD Dry**	B1 Min Wet	B3 Median Annual	B3 Median Dry

Table 6: Top five variables from the Recursive Feature Elimination model, at each scale (30m, 60m, 90m and 120m). SD: standard deviation.

6 Discussion

6.1 Landsat metrics, seasonality and scale

The accuracies obtained from the Landsat-derived woody cover maps varied according to the temporal window for which metrics were calculated. For single season data, the dry period metrics were the most useful. This result was anticipated due to the persistence of green shrubs into the dry season, compared with the grass layer (Fig 2; Naidoo et al., 2016). This makes woody cover easier to discriminate, compared to other periods where differences are less pronounced (Brandt et al., 2016). This can also explain the overestimation of wet season models in Fig 7, as the grass and wood layers are more difficult to separate and identify.

The distribution of errors also varied with seasonality. Dry season metrics performed better in areas of sparse woody cover (0-30% cover), whereas wet metrics offered marginal improvements in the 30-40% and 50-60% percentiles (Fig 12). This can be attributed to the dry season metrics having relatively a greater discriminatory power at sparse coverage where woody canopies are more distinct.

370 Furthermore, some areas of moderate woody coverage were under-predicted by dry season only
371 metrics. This can be attributed to the fact that some woody species are less persistent in dry
372 conditions (Subset B in Fig 7).

373 The best result from the multi-seasonal Landsat comparisons was the combination of dry and wet
374 season metrics. Although wet season metrics were the least effective mono-temporal models, when
375 combined with the contrasting dry season, the information covering the peak biomass period was
376 beneficial. This improvement was mainly limited to coverage between 10 and 70 % where each
377 percentile produced greater class accuracies than either single-season case, at both fine (30 m) and
378 coarse (120 m scales). In general, the multi-seasonal combinations improved prediction across the
379 full range of woody cover densities, with the 10-40% percentiles, at 120 m resolution, achieving the
380 highest-class accuracies. The ability to extract multiple sets of metrics from a time-series of images is
381 noteworthy, reducing to a certain extent the drawback of a temporally limited Landsat archive in
382 many savannah regions.

383 As fractional woody cover approaches the highest values (>70%), all models perform poorly with
384 no model achieving a percentile class accuracy of more than 56% (Fig 12). This is partly due to the
385 rare occurrence of this class, which affects the regression analysis. The poor accuracy for dense
386 woody savannahs has been noted by numerous other studies (e.g. Bucini et al., 2010, Naidoo et al.,
387 2016), and should be a priority for future studies.

388 We tested models at four scales: 30, 60, 90, and 120 m pixels. As pixel size increased, model
389 accuracies consistently improved (Figs 8 and 9). The largest improvement occurred with the initial
390 aggregation from 30 to 60 m, with a mean R^2 increase of $13.09\% \pm 0.9$, across the 13 models tested.
391 However, this change must be considered with the distribution of the input training values. At 30 m,
392 there is a relativity larger spread of values and a higher proportion of dense and sparse woody
393 coverage (Fig 5). Accordingly, this distribution is a more complicated endeavour for the regression
394 analysis, as indicated by the low class accuracies for high cover percentiles (Fig 12). Concurrently, the

395 greater proportion, and pixel purity, of sparsely (0-10%) wooded areas at 30 m result in comparably
396 high class accuracies for the first percentile class (Fig 12). Resampling to a coarser resolution reduces
397 the occurrence of dense woody coverage, due to central tendency, making the regression exercise
398 easier. This simplification is restricted to the 30 to 60 m aggregation with no visual or statistical
399 evidence that additional resampling improves the outcome of the regression. Further reductions in
400 the pixel resolution result in more modest but consistent improvements of $4.20\%\pm0.74$ and
401 $1.30\%\pm0.99$ in the R^2 when re-scaling from 60 to 90 m and from 90 to 120 m, respectively. At coarser
402 scales, artefacts from the Landsat processing are likely to be smoothed, as errors resulting from the
403 Scan Line Corrector failure and undetected clouds are minimised (Fig 7). Furthermore, despite the
404 high georeferencing accuracy of the datasets, errors from potential misalignment of the training
405 imagery and Landsat data may be more prevalent at 30 m and averaged at coarser scales. For many
406 regional-scale applications, land cover maps at 90 or 120 m may be sufficient, and an accuracy vs.
407 precision trade-off might be appropriate. Maps at 120 m may be more accurate, but have less fidelity
408 for detecting the clumps and canopies of dryland vegetation. This trade off may become more
409 pertinent with the availability of 10-20 m imagery from Sentinel-2 (Bastin et al., 2017) .

410 Overall, the accuracies achieved by the Landsat-based models are comparable to those of radar-
411 based studies at similar scales. Urbazaev et al., (2015) achieved R^2 values of 0.71 and 0.66 using
412 multiple and single season PALSAR images at 50 m resolution, respectively, whilst Naidoo et al.,
413 (2016) obtained R^2 of 0.8 and 0.81 using single-season PALSAR data at 105 m. Given our
414 considerably larger study area, our results are promising for regional-scale analysis, as the spatial
415 breadth, temporal depth, and rapid processing potential of the Landsat archive is unmatched by any
416 radar system (Kennedy et al., 2014, Roy et al., 2014). Our metrics-based approach outperforms the
417 various single date Landsat scenarios across multiple seasons achieved by Naidoo et al. (2016) who
418 reported R^2 values of 0.32-0.65 at 105 m resolution. There are clear benefits to quantifying seasonal
419 variability using metrics, as demonstrated by the high ranking of standard deviation layers (Table 6).
420 Furthermore, multi-seasonal metrics further improved results over multi-seasonal image

421 combinations. We attributed this refinement to two factors: firstly, metrics are more resistant to
422 bias incurred by rainfall and moisture variation; secondly, metrics such as standard deviation can
423 represent the temporal profile of the land cover, imitating time-series approaches. This is in
424 agreement with Müller et al. (2015), who found that annual metrics outperform best available pixel
425 composites for tropical savannahs in Brazil.

426 Large-area mapping of savannah systems remains a challenge due to high heterogeneity and
427 subjective biome classifications (Herold et al., 2008, Hüttich et al., 2011). Current approaches for
428 regional-scale mapping generally focus on best-available pixel composites for classification (Griffths
429 et al., 2013, White et al., 2014, Frantz et al., 2017). Due to the high temporal variation in savannahs,
430 this method is particularly vulnerable to bias effects caused by pixels being selected in different
431 phenological stages (Hüttich et al., 2011, Müller et al., 2015). We demonstrate that Landsat-based
432 spectral variability metrics offer a robust alternative for land cover mapping at large spatial scales,
433 applicable to epochal or annual analyses. South Africa possesses good availability of Landsat imagery
434 in the USGS archive, owing to the successful transfer of data from the Johannesburg receiving station,
435 active since 1980 (Wulder et al., 2015). However, in many savannah regions, such as the Sahel and
436 east Africa, the historical Landsat archive is sparse. By combining multiple years of observations, wall-
437 to-wall mapping should be possible even with low annual image availability. Furthermore,
438 segmenting a time-series into multiple temporal windows allows additional value to be extracted
439 from a single series of observations, potentially compensating for a relatively limited archive. The
440 high image acquisition rate of Landsat 8 relative to the historic Landsat archive, combined with
441 comparable imagery from the Sentinel-2 satellites, will result in improved temporal resolution for
442 optical imagery (Drusch et al., 2012, Roy et al., 2014). Increased observations should enable our multi-
443 seasonal metrics approach to be expanded by using more or smaller temporal windows, for example
444 the beginning or ending of the dry season. Evidence from MODIS-based studies suggests that this
445 refinement may allow increased discrimination of subtle land covers, such as densely wooded
446 savannahs, which are currently poorly mapped (Hüttich et al., 2009).

6.2 Landsat-PALSAR fusion

Integrating the Landsat metrics with L-band PALSAR backscatter had divergent impacts. Finer-scale maps (30 to 90 m) were negatively affected by the inclusion of radar, with the Landsat-only models outperforming their fused counterparts (Table 4). Comparably, the PALSAR-only models performed poorly, especially at fine-scales (Table 3). We attribute this to the high-level of noise in radar imagery at higher resolutions, as illustrated in Fig 13. Errors caused by factors such as speckle, moisture content and geolocation accuracy are far more prevalent in finer-scale radar data. Therefore, at 30 to 90 m pixel scales, the PALSAR imagery contains a weak signal-to-noise ratio, incurring a negative impact on the regression model. This is further reflected in the increasing ranks of radar variables in the Recursive Feature Elimination (RFE, Table 6). Accordingly, SAR-fusion reduced class accuracy by ~1% for area 20-60% coverage, at 30 m scales (Fig 12).Conversely, the coarse scale models (120 m) were consistently improved by the addition of PALSAR backscatter to the Landsat metrics, with the single-season combinations undergoing the greatest improvement. The lower improvements for the multi-seasonal scenarios indicates that some of the information contained in radar backscatter can be obtained from multi-seasonal metrics. The inclusion of L-band radar had the highest impact on sparse woody cover classes (0-30%). Within these classes, inclusion of the SAR variables increased balanced accuracies by 1-9% and 1-2%, at 120 and 30 m scales, respectively (Fig 12). Visual examination of the prediction subset maps indicates that this improvement is due to the SAR fusion correcting for overestimations when there is 0 - 20 % woody cover (e.g. the central pivot irrigation fields in Subset A of Fig 7).

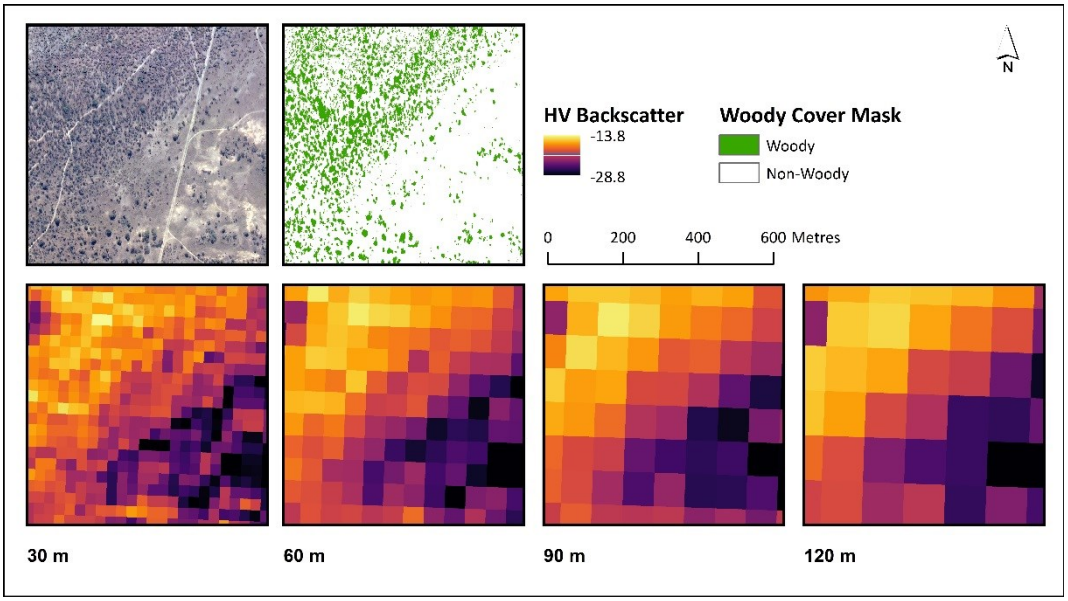

Figure 13: Subsets of HV polarized PALSAR backscatter across a grassland-shrub transition at different resolutions

Multi-sensor fusion approaches are becoming more popular, due to an increase in the number of operational sensors and the open-access data policies. The improvements at coarse scales are in line with those found in other studies employing SAR and Landsat data together (Bucini et al., 2010, Naidoo et al., 2016). However, this study is the first to quantify the effect and mechanism of this fusion across multiple seasons and scales. The accuracies of the PALSAR-only models generated here are lower than other South African studies (e.g. Naidoo et al., 2016, Urbazaev et al., 2015). We attribute this to the much larger and heterogeneous study area that we cover, encompassing human modified landscapes where the other two studies were confined within the Kruger National Park. The source of training data could also have affected the accuracy of our PALSAR-based estimates: we employ aerial photographs while Naidoo et al. (2016) and Urbazaev et al. (2015) use more accurate characterisations from the field or from LiDAR sources. It should also be noted that our study used a mosaicked ALOS PALSAR layer produced from images acquired across a three month window (1st July - 3rd October), including two images acquired in the previous year. Seasonal effects, such as canopy density and moisture content, may prevent the mosaicked images from being artefact-free. Alternatively, the global-scale processing undertaken in the creation of the mosaicked PALSAR layer,

such as speckle reduction and topographic normalisation, may reduce the fidelity of backscatter measurements when compared to scene-specific methods applied elsewhere (e.g. Naidoo et al., 2016, Urbazaev et al., 2015). Furthermore, multi-sensor fusion has a potential for image miss-registration errors between the imagery (Lehmann et al., 2015).

Although overall model accuracies are only moderately changed by the inclusion of L-band SAR data, the consistent allocation of improvements at low densities of woody cover may be highly relevant to semi-arid savannah case studies. The process of shrub encroachment into grasslands is a major threat to the livelihoods of many pastoralists in the developing world. For prevention and remediation to be successful, action must be taken as early as possible. The periodic monitoring of sparsely wooded savannahs, which are vulnerable to shrub encroachment, is therefore a pressing requirement. For this purpose, the fusion of PALSAR and Landsat imagery is beneficial, offering a higher likelihood of timely change detection than single-sensor approaches. In the coming years, fusion techniques based C-band radar from Sentinel-1 may offer good promise, owing to the 12 day revisit time.

6.3 Merit of variable reduction methods

To ascertain the value of variable reduction methods we applied a Recursive Feature Elimination (RFE) on out 92 variable dataset. The RFE produced the best preforming model at all scales, compared to all Landsat and Landsat-PALSAR fusion cases (Fig 11). In general, the number of variables used in the RFE models decreased with aggregation: we attribute the requirement of less variables at coarser resolutions to improvements in signal-to-noise ratios as noisier layers are smoothed. Dimension reduction methods are also useful for highlighting the type of variables that contain useful information for the model building. The high ranking of standard deviation - a proxy for seasonal variability highlights the importance of temporal information for woody cover mapping.

As both the number of active sensors and the availability of open data archives increase, remote sensing analyses are using high-dimensional datasets. The utility of variable selection or dimension reduction methods will inevitably increase in order to deal with the increasing data volume. Currently, these tools are primarily used in hyperspectral analyses, but are underutilised in other areas (Pal and Foody 2010). The fact that the RFE was able to automate the process of selecting a superior model highlights the potential of automating model construction using machine learning methods that may currently be underused (Meyer et al., 2016). At large-scales, mapping land cover with fewer variables can drastically reduce processing time, leaving unnecessary variables out can therefore be useful for computing and statistical purposes.

7 Conclusions

We tested the potential of Landsat-derived spectral variability metrics and PALSAR composites for mapping woody coverage, in southern African savannahs. We compared the role of seasonal compositing period, and the effect of multi-sensor fusion through the addition of ALOS PALSAR backscatter to the Landsat layers. Furthermore, we investigated the role of pixel scale on map accuracy, and the potential of variable selection methods for automating the model building process.

We draw a number of conclusions from our modelling scenarios. Firstly, Landsat metrics can produce highly accurate maps of fractional cover in savannas, with dry season imagery being the preferred temporal window. Further improvements can be made by combining multi-seasonal metrics, derived from two contrasting seasons. In particular, integrating dry and wet season layers produced good improvements in map accuracy. Secondly, the fusion of Landsat and PALSAR layers is not always beneficial. At fine scales (30-60 m), L-band SAR integration reduced model performance consistently, potentially due to the high level of noise inherent to radar data,

particularly in savannahs. Conversely, at the 120 m scale, the addition of PALSAR was beneficial, particularly for areas with less than 30% coverage, and for some models at 90 m scales as well. Finally, the use of a recursive feature elimination automated variable selection process was very efficient in constructing an accurate parsimonious model, producing the most effective model at every scale examined whilst reducing the number of variables used to of 57 out of 90.

In summary, Landsat metrics offer a suitable option for regional-scale mapping of savannah woody cover, and should allow decadal scale analysis of land cover changes. The use of multi-seasonal composites are particularly promising for accurate fractional woody cover mapping. For contemporary monitoring, the fusion of Landsat metrics with L-band radar is recommended for areas with lower woody cover densities, and particularly for the rapid detection of shrub encroachment into grass-dominated savannahs. Future studies will benefit from automated variable reduction approaches and the increased image acquisition rates from the Sentinel constellation, that feature both radar (C-Band) and optical satellites.

Acknowledgements

TH is funded by a Manchester Metropolitan University (MMU) Research Fellowship. ES is supported by an EU FP7 Marie Curie Career Integration Grant (PCIG12-GA-2012-3374327). We are grateful to the USGS, JAXA, and the NGI for providing the data used in this study. The authors declare no personal or financial conflicts of interest.

References

Armston, J. D., R. J. Denham, Danaher, T. J. Scarth, P. F. Mo et, and N Trevor (2009). Prediction and validation of foliage projective cover from Landsat-5 TM and Landsat-7 ETM+ imagery. Journal of Applied Remote Sensing 3.(033540).

554 Bastin, J.F., Berrahmouni, N., Grainger, A., Maniatis, D., Mollicone, D., Moore, R., Patriarca, C.,
555 Picard, N., Sparrow, B., Abraham, E.M. and Aloui, K., 2017. The extent of forest in dryland
556 biomes. Science, 356(6338), pp.635-638.

557 Brandt, M., P. Hiernaux, T. Tagesson, A. Verger, K. Rasmussen, A. A. Diouf, C. Mbow, E. Mougin,
558 and R. Fensholt (2016). Woody plant cover estimation in drylands from Earth Observation based
559 seasonal metrics. Remote Sensing of Environment 172, 28 38.

560 Breiman, L. (2001). Random forests. Machine learning 45.(1), 5 32.

561 Bucini, G, N. Hanan, R. Boone, I. Smit, S Saatchi, M. Lefsky, and G. Asner (2010). Woody
562 fractional cover in Kruger National Park, South Africa: remote-sensing-based maps and
563 ecological insights. Ecosystem function in savannas: measurement and modelling at landscape
564 to global scales. Ed. by M. J. Hill and N. P. Hanan. Boca Raton, Florida: CRC Press. Chap. 11, pp.
565 219 238.

566 Brandt, M., Rasmussen, K., Peñuelas, J., Tian, F., Schurgers, G., Verger, A., Mertz, O., Palmer, J.R.
567 and Fensholt, R., 2017. Human population growth offsets climate-driven increase in woody
568 vegetation in sub-Saharan Africa. Nature Ecology & Evolution, 1(4), pp.s41559-017.

569 Carlson, T. N. and D. A. Ripley (1997). On the relation between NDVI, fractional vegetation
570 cover, and leaf area index. Remote sensing of Environment 62.(3), 241 252.

571 Drusch, M, U Del Bello, S Carlier, O Colin, V Fernandez, F Gascon, B Hoersch, C Isola, P Laberinti,
572 P Martimort, et al., (2012). Sentinel-2: ESA's optical high-resolution mission for GMES
573 operational services. Remote Sensing of Environment 120, 25 36.

574 Frantz, D., Röder, A., Stellmes, M. and Hill, J. (2017) Phenology-adaptive pixel-based
575 compositing using optical earth observation imagery. Remote Sensing of Environment 190. 331-
576 347.

577 Guyon, I. and Elisseeff, A., 2003. An introduction to variable and feature selection. Journal of
578 machine learning research, 3.1157-1182.

579 Grifiths, P., S. Van Der Linden, T. Kuemmerle, and P. Hostert (2013). A pixel-based Landsat
580 compositing algorithm for large area land cover mapping. IEEE Journal of Selected Topics in
581 Applied Earth Observations and Remote Sensing 6.(5), 2088 2101.

582 Guerschman, J.P., Hill, M.J., Renzullo, L.J., Barrett, D.J., Marks, A.S. and Botha, E.J., (2009).
583 Estimating fractional cover of photosynthetic vegetation, non-photosynthetic vegetation and
584 bare soil in the Australian tropical savanna region upscaling the EO-1 Hyperion and MODIS
585 sensors. Remote Sensing of Environment, 113(5),928-945.

586 Guyon, I., J. Weston, S. Barnhill, and V. Vapnik (2002). Gene selection for cancer classification
587 using support vector machines. Machine learning 46.(1-3), 389 422.

588 Herold, M, P Mayaux, C. Woodcock, A Baccini, and C Schmullius (2008). Some challenges in
589 global land cover mapping: An assessment of agreement and accuracy in existing 1 km datasets.
590 Remote Sensing of Environment 112.(5), 2538 2556.

591 Higginbottom, T. P. and E. Symeonakis (2014). Assessing Land Degradation and Desertification
592 Using Vegetation Index Data: Current Frameworks and Future Directions. Remote Sensing
593 6.(10), 9552 9575.

Hijmans, R. J., J. van Etten, M. Mattiuzzi, M. Sumner, J. A. Greenberg, O. P. Lamigueiro, A. Bevan, E. B. Racine, A. Shortridge, and M. R. J. Hijmans (2015). raster: Geographic Data Analysis and Modelling. R package version 2.3-40.

Hostert, P., Griffiths, P., van der Linden, S. and Pflugmacher, D., 2015. Time series analyses in a new era of optical satellite data. In *Remote Sensing Time Series* (pp. 25-41). Springer International Publishing.

Huttich, C., U. Gessner, M. Herold, B. J. Strohbach, M. Schmidt, M. Keil, and S. Dech (2009). On the suitability of MODIS time series metrics to map vegetation types in dry savanna ecosystems: A case study in the Kalahari of NE Namibia. Remote Sensing 1.(4), 620 643.

Huttich, C., M. Herold, M. Wegmann, A. Cord, B. Strohbach, C. Schmullius, and S. Dech (2011). Assessing effects of temporal compositing and varying observation periods for large-area landcover mapping in semi-arid ecosystems: Implications for global monitoring. Remote Sensing of Environment 115.(10), 2445 2459.

Gorelick, N., Hancher, M., Dixon, M., Ilyushchenko, S., Thau, D. and Moore, R., 2017. Google Earth Engine: Planetary-scale geospatial analysis for everyone. Remote Sensing of Environment.

James, G., D. Witten, T. Hastie, and R. Tibshirani (2013). An introduction to statistical learning. Springer.

Joseph, J and Devadas, (2015) Detection of rooftop regions in rural areas using Support Vector Machine. International Journal of Science Research Engineering 4 549–553

Kennedy, R.E., Andréfouët, S., Cohen, W.B., Gómez, C., Griffiths, P., Hais, M., Healey, S.P., Helmer, E.H., Hostert, P., Lyons, M.B. and Meigs, G.W., Pflugmacher, D., Phinn, S.R., Powell, S.L., Scarth, P., Sen, S., Schroeder, T.A., Schneider, A., Sonnenschein, R., Vogelmann, J.E., Wulder, M.A., Zhu, Z. (2014). Bringing an ecological view of change to Landsat based remote sensing. Frontiers in Ecology and the Environment 12.(6), 339 346.

Kottek, M., J. Grieser, C. Beck, B. Rudolf, and F. Rubel (2006). World map of the Koppen-Geiger climate classification updated. Meteorologische Zeitschrift 15.(3), 259 263.

Kuhn, M. (2015). caret: Classification and Regression Training. R package version 6.0-52.

Kuhn, M. and K. Johnson (2013). Applied predictive modelling. Springer.

Leutner, B. and N. Horning (2016). RStoolbox: Tools for Remote Sensing Data Analysis. R package version 0.1.4.

Lehmann EA, Caccetta P, Lowell K, Mitchell A, Zhou ZS, Held A, Milne T, Tapley I (2015). SAR and optical remote sensing: Assessment of complementarity and interoperability in the context of a large-scale operational forest monitoring system. Remote Sensing of Environment (156). 335-348.

Liaw, A. and M. Wiener (2002). Classification and regression by randomForest. R news 2.(3), 18 22.

Lucas, R. M., N. Cronin, M. Moghaddam, A. Lee, J. Armston, P. Bunting, and C. Witte (2006). Integration of radar and Landsat-derived foliage projected cover for woody regrowth mapping, Queensland, Australia. Remote Sensing of Environment 100.(3), 388 406.

633 Ludwig, A, H Meyer, and T Nauss (2016). Automatic classification of Google Earth images for a
634 larger scale monitoring of bush encroachment in South Africa. International Journal of Applied
635 Earth Observation and Geoinformation.

636 Main, R., R. Mathieu, W. Kleynhans, K. Wessels, L. Naidoo, and G. P. Asner (2016). Hyper-
637 temporal C-band SAR for baseline woody structural assessments in deciduous savannas.
638 Remote Sensing 8.(8), 661.

639 Mathieu, R. et al., (2013). Toward structural assessment of semi-arid African savannahs and
640 woodlands: The potential of multitemporal polarimetric RADARSAT-2 beam images. Remote
641 Sensing of Environment 138, 215 231.

642 Meyer, H., M. Katurji, T. Appelhans, M. U. Muller, T. Nauss, P. Roudier, and P. Zawar-Reza
643 (2016). Mapping Daily Air Temperature for Antarctica Based on MODIS LST. Remote Sensing
644 8.(9), 732.

645 Mitchard, E., S. Saatchi, I. Woodhouse, G Nangendo, N. Ribeiro, M Williams, C. Ryan, S. Lewis, T.
646 Feldpausch, and P Meir (2009). Using satellite radar backscatter to predict aboveground woody
647 biomass: A consistent relationship across four different African landscapes. Geophysical
648 Research Letters 36.(23).

649 Moore, R.T. and Hansen, M.C., (2011) Google Earth Engine: a new cloud-computing platform for
650 global-scale earth observation data and analysis. AGU Fall Meeting Abstracts..

651 Mucina, L and M. Rutherford, eds. (2006). The vegetation of South Africa, Lesotho and
652 Swaziland. Pretoria: South African National Biodiversity Institute.

653 Muller, H., P. Ru n, P. Grifiths, A. J. B. Siqueira, and P. Hostert (2015). Mining dense Landsat time
654 series for separating cropland and pasture in a heterogeneous Brazilian savanna landscape.
655 Remote Sensing of Environment 156, 490 499.

656 Naidoo, L., R. Mathieu, R. Main, W. Kleynhans, K. Wessels, G. Asner, and B. Leblon (2015).
657 Savannah woody structure modelling and mapping using multi-frequency (X-, C-and L-band)
658 Synthetic Aperture Radar data. ISPRS Journal of Photogrammetry and Remote Sensing 105, 234
659 250.

660 Naidoo, L., R. Mathieu, R. Main, K. Wessels, and G. P. Asner (2016). L-band Synthetic Aperture
661 Radar imagery performs better than optical datasets at retrieving woody fractional cover in
662 deciduous, dry savannahs. International Journal of Applied Earth Observation and
663 Geoinformation 52, 54 64.

664 Naito, A. T. and D. M. Cairns (2011). Patterns and processes of global shrub expansion. Progress
665 in Physical Geography 35.(4), 423 442.

666 National Geo-spatial Information (2017) Colour Digital Aerial Imagery [online].
667 *http://www.ngi.gov.za/index.php/what-we-do/aerial-photography-and-imagery/35-colour-*
668 *digital-aerial-imagery-at-0-5m-gsd-2008-2016-and-0-25m-gsd-2017-current*

669 Olsson, A. D., W. J. van Leeuwen, and S. E. Marsh (2011). Feasibility of invasive grass detection
670 in a desertscrub community using hyperspectral field measurements and Landsat TM imagery.
671 Remote Sensing 3.(10), 2283 2304.

672 Pal, M. and G. M. Foody (2010). Feature selection for classification of hyperspectral data by
673 SVM. IEEE Transactions on Geoscience and Remote Sensing 48.(5), 2297 2307.

674 Prince, S.D. and Astle, W.L., 1986. Satellite remote sensing of rangelands in Botswana I. Landsat
675 MSS and herbaceous vegetation. International Journal of Remote Sensing, 7(11) .1533-1553.

676 Pollard, S., C. Shackleton, and J. Carruthers (2003). Beyond the fence: people and the lowveld
677 landscape. The Kruger experience: Ecology and management of savanna heterogeneity. Ed. by J.
678 T. Du Toit, K. H. Rogers, and H. C. Biggs. Washington: Island Press. Chap. 7, pp. 422 446.

679 R Core Team (2015). R: A Language and Environment for Statistical Computing. R Foundation for
680 Statistical Computing. Vienna, Austria.

681 Reiche, J., Lucas, R., Mitchell, A.L., Verbesselt, J., Hoekman, D.H., Haarpaintner, J., Kellndorfer,
682 J.M., Rosenqvist, A., Lehmann, E.A., Woodcock, C.E. and Seifert, F.M., 2016. Combining satellite
683 data for better tropical forest monitoring. Nature Climate Change, 6(2), p.120.

684 Rosenqvist, A., M. Shimada, N. Ito, and M. Watanabe (2007). ALOS PALSAR: A pathfinder
685 mission for global-scale monitoring of the environment. IEEE Transactions on Geoscience and
686 Remote Sensing 45.(11), 3307 3316.

687 Roy, D. P., M. Wulder, T. Loveland, C. Woodcock, R. Allen, M. Anderson, D Helder, J. Irons, D.
688 Johnson, R Kennedy, et al., (2014). Landsat-8: Science and product vision for terrestrial global
689 change research. Remote Sensing of Environment 145, 154 172.

690 Sankaran, M., N. P. Hanan, R. J. Scholes, J. Ratnam, D. J. Augustine, B. S. Cade, J. Gignoux, S. I.
691 Higgins, X. Le Roux, and F. Ludwig (2005). Determinants of woody cover in African savannas.
692 Nature 438.(7069), 846 849.

693 Scholes, R., N Gureja, M Giannecchinni, D Dovie, B Wilson, N Davidson, K Piggott, C McLoughlin,
694 K Van der Velde, A Freeman, et al., (2001). The environment and vegetation of the flux
695 measurement site near Skukuza, Kruger National Park. Koedoe 44.(1), 73 83.

696 Shimada, M. and T. Ohtaki (2010). Generating large-scale high-quality SAR mosaic datasets:
697 Application to PALSAR data for global monitoring. IEEE Journal of Selected Topics in Applied
698 Earth Observations and Remote Sensing 3.(4), 637 656.

699 Shimada, M., T. Itoh, T. Motooka, M. Watanabe, T. Shiraishi, R. Thapa, and R. Lucas (2014). New
700 global forest/non-forest maps from ALOS PALSAR data (2007 2010). Remote Sensing of
701 Environment 155, 13 31.

702 Staben, G.W., Lucieer, A., Evans, K.G., Scarth, P. and Cook, G.D., 2016. Obtaining biophysical
703 measurements of woody vegetation from high resolution digital aerial photography in tropical
704 and arid environments: Northern Territory, Australia. International Journal of Applied Earth
705 Observation and Geoinformation, 52, pp.204-220.

706 Skowno, A.L., Thompson, M.W., Hiestermann, J., Ripley, B., West, A.G. and Bond, W.J., 2017.
707 Woodland expansion in South African grassy biomes based on satellite observations (1990–
708 2013): general patterns and potential drivers. Global change biology, 23(6), pp.2358-2369.

709 Stevens, N., Lehmann, C.E., Murphy, B.P. and Durigan, G., 2017. Savanna woody encroachment
710 is widespread across three continents. Global change biology, 23(1), pp.235-244.

711 Tian, F., Brandt, M., Liu, Y.Y., Rasmussen, K. and Fensholt, R., 2017. Mapping gains and losses in
712 woody vegetation across global tropical drylands. Global change biology, 23(4), pp.1748-1760.

Urbazaev, M., C. Thiel, R. Mathieu, L. Naidoo, S. R. Levick, I. P. Smit, G. P. Asner, and C. Schmullius (2015). Assessment of the mapping of fractional woody cover in southern African savannas using multi-temporal and polarimetric ALOS PALSAR L-band images. Remote Sensing of Environment 166, 138 153.

Wessels, K. J., M. S. Colgan, B. F. N. Erasmus, G. P. Asner, W. C. Twine, R. Mathieu, J. A. N. Van Aardt, J. T. Fisher, and I. P. J. Smit (2013). Unsustainable fuelwood extraction from South African savannas. Environmental Research Letters 8.(1).

Worden, N., (1994). The making of modern South Africa: conquest, segregation, and apartheid. Juta and Company Ltd.

White, J., M. Wulder, G. Hobart, J. Luther, T Hermosilla, P Griffiths, N. Coops, R. Hall, P Hostert, A Dyk, et al., (2014). Pixel-based image compositing for large-area dense time series applications and science. Canadian Journal of Remote Sensing 40.(3), 192 212.

Wulder, M. A., J. C. White, T. R. Loveland, C. E. Woodcock, A. S. Belward, W. B. Cohen, E. A. Fosnight, J. Shaw, J. G. Masek, and D. P. Roy (2015). The global Landsat archive: Status, consolidation, and direction. Remote Sensing of Environment 185, 271 283.

Zhong, L., P. Gong, and G. S. Biging (2014). Efficient corn and soybean mapping with temporal extendibility: A multi-year experiment using Landsat imagery. Remote Sensing of Environment 140, 1 13.

Zhu, Z., J. Bi, Y. Pan, S. Ganguly, A. Anav, L. Xu, A. Samanta, S. Piao, R. R. Nemani, and R. B. Myneni (2013). Global data sets of vegetation leaf area index (LAI) 3g and Fraction of photosynthetically Active Radiation (FPAR) 3g derived from Global Inventory Modelling and Mapping Studies (GIMMS) Normalized Difference Vegetation Index (NDVI3g) for the period 1981 to 2011. Remote Sensing 5.(2), 927 948.

Zhu, Z. and Woodcock, C.E., (2012). Object-based cloud and cloud shadow detection in Landsat imagery. Remote Sensing of Environment, 118,.83-94.

Appendix

Table A1 Woody cover mask classification accuracies.

Mask Number	Date	Accuracy	Sensitivity	Specificity

1	19/04/2009	0.74	0.73	0.75
2	30/04/2009	0.85	0.88	0.80
3	01/05/2009	0.85	0.88	0.80
4	07/08/2008	0.87	0.87	0.88
5	23/06/2008	0.85	0.86	0.85
6	01/06/2008	0.92	0.88	0.95
Positive Class: Woody Cover				

748

749